NEUROSCIENCE

Locally coordinated synaptic plasticity of visual cortex neurons in vivo

Sami El-Boustani[1]*†‡, Jacque P. K. Ip[1]†, Vincent Breton-Provencher[1], Graham W. Knott[2], Hiroyuki Okuno[3]§, Haruhiko Bito[4], Mriganka Sur[1]*

Plasticity of cortical responses in vivo involves activity-dependent changes at synapses, but the manner in which different forms of synaptic plasticity act together to create functional changes in neurons remains unknown. We found that spike timing–induced receptive field plasticity of visual cortex neurons in mice is anchored by increases in the synaptic strength of identified spines. This is accompanied by a decrease in the strength of adjacent spines on a slower time scale. The locally coordinated potentiation and depression of spines involves prominent AMPA receptor redistribution via targeted expression of the immediate early gene product Arc. Hebbian strengthening of activated synapses and heterosynaptic weakening of adjacent synapses thus cooperatively orchestrate cell-wide plasticity of functional neuronal responses.

Neuronal circuits in the brain are subject to changes driven by sensory inputs (*1*, *2*) or motor learning (*3*–*5*), causing cells to modify their responses to individual inputs while maintaining a stable level of activity (*6*). Homeostatic plasticity stabilizes the output firing rate of single neurons by uniformly scaling up or down the strength of all synapses (*6*, *7*). Other forms of compensatory plasticity can also act locally at dendritic stretches (*8*–*14*) or even at single synapses (*15*–*17*). Synaptic potentiation at specific dendritic locations could be coordinated with heterosynaptic depression of nearby synapses within short stretches of the same dendrite to cooperatively implement functional plasticity of single-cell responses (*18*). It is unknown whether locally coordinated synaptic plasticity occurs in vivo and whether it has a role in shaping neuronal responses.

Cortical plasticity induced by sensory deprivation or enrichment (*2*) results in large-scale functional and structural changes across many neurons and synapses. We developed a controlled paradigm for inducing plasticity at identified synapses on single neurons in the primary visual cortex (V1) of awake juvenile mice (postnatal day 28 to 35). We reasoned that pre-before-post pairing at specific synapses, via visual stimuli presented at a target location closely followed by channelrhodopsin-2 (ChR2)–driven spiking of an individual neuron, would induce Hebbian potentiation of excitatory synapses responding to the target stimulus and consequently shift the receptive field at the soma (Fig. 1, A and B). We characterized excitatory synaptic inputs to V1 layer 2/3 neurons in response to sparse noise stimuli (*19*) (Fig. 1, C to E). Evoked excitatory postsynaptic currents (EPSCs) typically responded to stimulus onset or offset (Fig. 1F). Onset responses lasted for about 200 ms with a peak response at 65 to 130 ms (mean, 96.3 ± 7.4 ms; n = 8 neurons). To ensure that the peak synaptic input led the ChR2 action potential, we induced postsynaptic spiking 150 ms after visual stimulus onset to potentiate responses to the target stimulus and avoid post-before-pre pairing. Such ChR2-induced spiking corresponded to a peak excitatory postsynaptic potential to spike time difference of 20 to 85 ms, which overlaps with time windows used in previous studies to induce response potentiation (*20*, *21*).

To induce and measure receptive field plasticity over extended periods of time, we electroporated the calcium indicator mRuby2-P2A-GCaMP6s (*22*) and the opsin ChR2-mCherry (*23*) in single neurons (*19*) (Fig. 1, G and H). ChR2 allowed precise control of neuronal spikes (Fig. 1I; n = 7 neurons; number of spikes per pulse = 1.2 ± 0.32). We used the GCaMP6s signal to map receptive fields measured at the soma (Fig. 1, J and K, and fig. S1, A and B). We then determined a target location close to the peak receptive field response location. Repeated presentations of the target stimulus were paired with single blue light pulses to elicit ChR2 spikes (60 pairings). Receptive fields were measured again 1 to 2 hours postpairing. For most neurons, the receptive field center of mass shifted toward the target stimulus (Fig. 1, K and L). These changes were not observed when ChR2 stimulation was not paired with the target stimulus (*19*) (Fig. 1L). Receptive field shifts could not be explained by changes in eye position (fig. S2) and did not induce functional changes in the network (fig. S3). Receptive field shifts could also be achieved with other pairing rates and durations (fig. S4).

We next investigated the structural basis of receptive field plasticity at the synaptic level. We used dendritic spine volume changes as a structural proxy for long-term potentiation or depression (*24*–*26*). By comparing dendritic spines pre- and postpairing, we observed bidirectional volume changes within dendritic stretches (Fig. 2A). These changes were not caused by drifts in the imaging planes (fig. S5). Spines exhibiting structural long-term potentiation (sLTP) or depression (sLTD) were compared with those in control experiments in the absence of ChR2 ($ChR2^-$; Fig. 2, B and C). We quantified changes in spine volume by using the normalized difference (δV) between the integrated spine fluorescence signal relative to the shaft pre- and postpairing, and we defined a threshold for pairing-induced sLTP and sLTD in $ChR2^+$ neurons ($\delta V = \pm 0.25$, corresponding to spines that exceeded the 97th percentile of the $ChR2^-$ distribution; fig. S6). We then backtracked the temporal evolution of significantly potentiated or depressed spines (Fig. 2D). sLTP spines rapidly increased in volume immediately after pairing, and this was followed by a moderate increase over the next 2 hours. In contrast, sLTD spines showed an initial small decrease in volume that was amplified over the next 2 hours until the average volume change for sLTD and sLTP spines became approximately balanced. The density of sLTD spines was significantly correlated with, and was greater than, the density of sLTP spines in individual dendrites (Fig. 2E). sLTD spine density was significantly larger at short sLTP-sLTD distances (*19*), indicating that sLTD spines were preferentially located around sLTP spines (Fig. 2F).

We reconstructed stretches of dendrite from $ChR2^+$ and $ChR2^-$ neurons with electron microscopy (EM) (Fig. 2, G and J) and compared spines that were well isolated in two-photon images (*19*). All two-photon–imaged spines on these dendrites were identified by EM. For both the $ChR2^+$ and $ChR2^-$ dendrite, EM spine volumes were highly correlated with the spine fluorescence signal postpairing (Fig. 2, H and K). Consistent with the observation that structural plasticity caused by pairing resulted in both increases and decreases of spine volumes in $ChR2^+$ neurons, whereas volumes remained stable in $ChR2^-$ neurons, prepairing signals showed significantly larger dispersion around the best fit for the $ChR2^+$ dendrite (Fig. 2H) but were equivalent to postpairing signals for the $ChR2^-$ dendrite (Fig. 2K). EM spine volume was highly correlated with synaptic surface area, consistent

[1]Department of Brain and Cognitive Sciences, Picower Institute for Learning and Memory, Massachusetts Institute of Technology, Cambridge, MA 02139, USA. [2]Bio Electron Microscopy Laboratory, School of Life Sciences, École Polytechnique Fédérale de Lausanne, Lausanne 1015, Switzerland. [3]Medical Innovation Center, Kyoto University Graduate School of Medicine, Sakyo-ku, Kyoto 606-8507, Japan. [4]Department of Neurochemistry, Graduate School of Medicine, The University of Tokyo, Hongo 7-3-1, Bunkyo-ku, Tokyo 113-0033, Japan.
***Corresponding author. Email: msur@mit.edu (M.S.); elbousta@mit.edu (S.E.-B.)** †These authors contributed equally to this work. ‡Present address: Brain Mind Institute, School of Life Sciences, Ecole Polytechnique Fédérale de Lausanne, Lausanne 1015, Switzerland. §Present address: Department of Biochemistry and Molecular Biology, Graduate School of Medical and Dental Sciences, Kagoshima University, 8-35-1 Sakuragaoka, Kagoshima 890-8544, Japan.

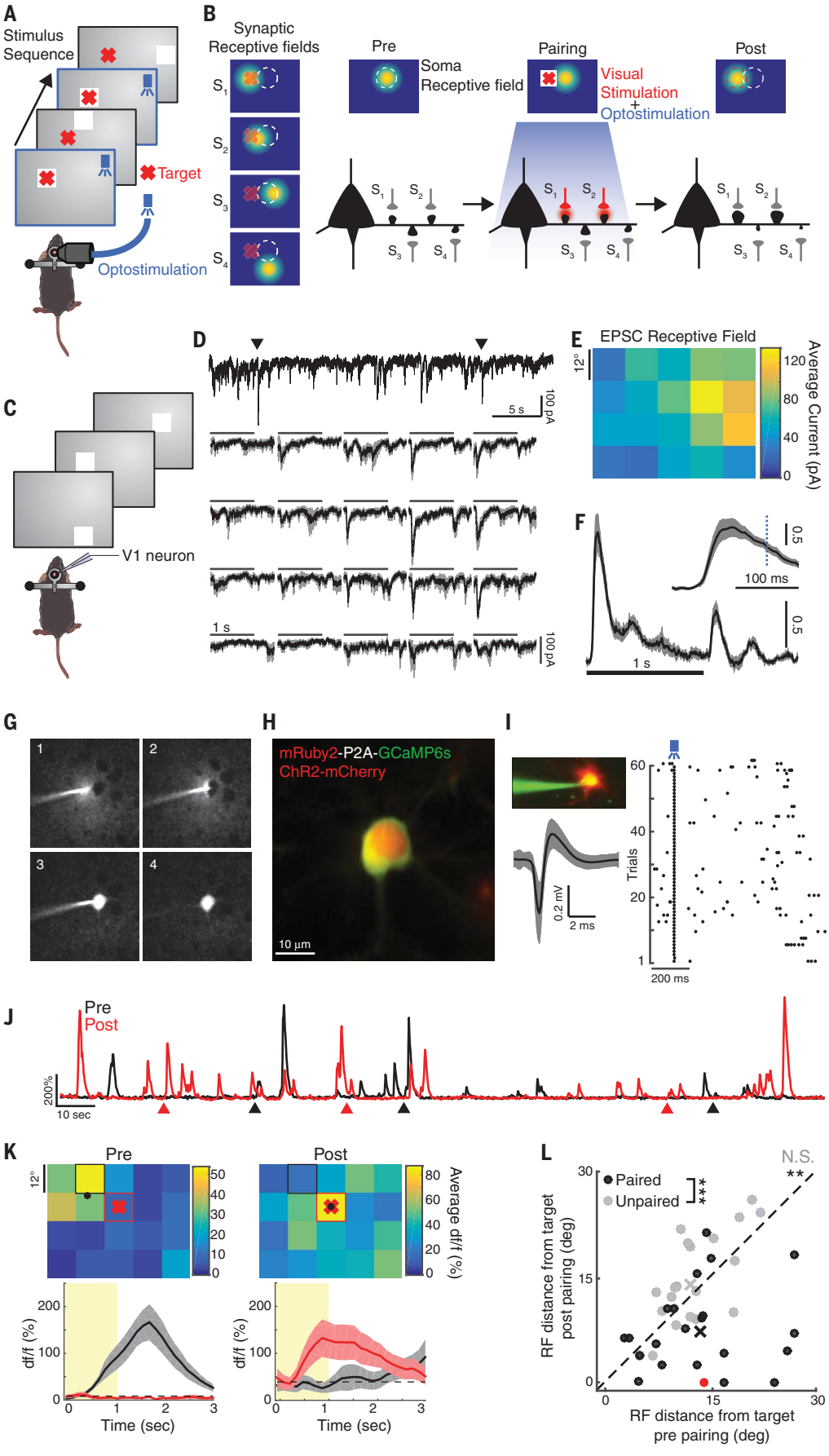

Fig. 1. Induction of receptive field plasticity in V1 neurons. (**A**) Pairing protocol (white squares, visual stimuli). (**B**) Effect of pairing on a neuron's receptive field and its dendritic spines (S_1 to S_4). (**C**) Whole-cell recording during sparse noise stimuli. (**D**) Top, excitatory current trace of a recorded neuron. Bottom, average EPSC for each stimulus location (gray shading, SEM). (**E**) Receptive field obtained by averaging EPSCs between 50 and 150 ms. (**F**) EPSC in *z*-score averaged over all neurons and stimulus locations (n = 8 neurons). Gray shading, SEM; dotted blue line, 150 ms. (**G**) Single-cell electroporation in vivo. (**H**) Neuron expressing mRuby2-P2A-GCaMP6s and ChR2-mCherry. (**I**) Loose-patch recording of a ChR2$^+$ neuron spiking to single blue light pulses. Spike waveforms are shown (gray shading, standard deviation). (**J**) Calcium df/*f* (fluorescence signal changes relative to baseline) traces obtained from soma. Arrowheads, onset of visual stimuli, presented prepairing at the preferred location (black) and postpairing at the target location (red). (**K**) Top, receptive fields from the traces in (J). Preferred stimulus locations are shown with black (pre) and red (post) squares. Black dots, center of mass. Red crosses, target stimulus. Bottom, response time course in squared locations. Shaded areas, SEM. Black dashed line, baseline df/*f* level. (**L**) Distance between the target and receptive field center of mass pre- and postpairing (black; n = 22 neurons; N = 23 mice; paired Wilcoxon test, $^{**}P < 0.01$). Red dot, example in (K). X, average shift. Control neurons with unpaired ChR2-visual stimulation are shown in gray (n = 21 neurons; N = 11 mice; P = 0.06; N.S., not significant). Receptive field shifts were significantly different between paired and unpaired populations (unpaired Kruskal-Wallis test, $^{***}P < 0.001$).

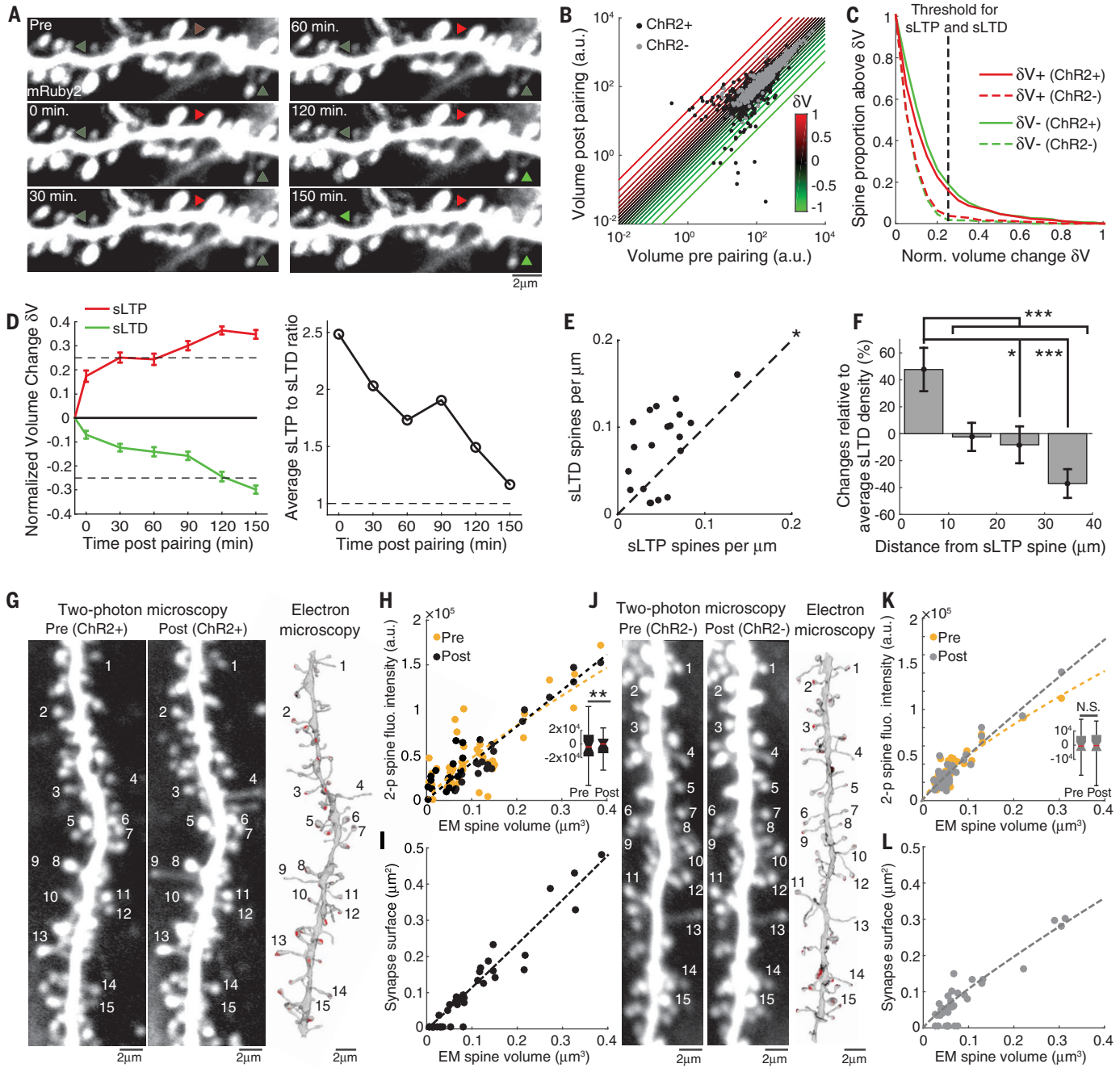

Fig. 2. Hebbian potentiation and heterosynaptic depression in stretches of dendrite. (**A**) Time-lapse dendritic imaging. Arrowheads correspond to sLTP (red) and sLTD (green) spines. (**B**) Spine volumes pre- and postpairing (>2 hours) for ChR2$^+$ (n = 1498 spines) and ChR2$^-$ (n = 845 spines) neurons. a.u., arbitrary units. (**C**) Proportion of enlarged (δV+) and shrunken (δV–) spines above different δV values (variance F-test between ChR2$^+$ and ChR2$^-$, $P < 0.001$). Black dashed line, sLTP and sLTD threshold $\delta V = \pm 0.25$. (**D**) Left, average normalized volume change over time for sLTP (n = 110) and sLTD (n = 98) spines. Dashed lines, threshold. Right, sLTP-to-sLTD volume change ratio. (**E**) sLTP and sLTD spine density per dendrite (n = 20 dendrites; Pearson coefficient = 0.55, $P < 0.05$; paired Wilcoxon test, *$P < 0.05$). (**F**) sLTD spine density variation relative to the mean as a function of distance from sLTP spines [n = 103 sLTP spines; one-way analysis of variance (ANOVA), $P < 0.01$; unpaired Kruskal-Wallis test, ***$P < 0.001$ and *$P < 0.05$ with Bonferroni correction]. (**G**) ChR2$^+$ dendrite imaged pre- and postpairing and reconstructed by EM after the experiment, postpairing. (**H**) Spine volume measured with EM compared to two-photon fluorescence signal [n = 36 spines; EM versus post, coefficient of determination (r^2) = 0.85; EM versus pre, r^2 = 0.57]. Lines depict best-fit power functions. Inset, distribution of fit residuals (unpaired variance F-test, **$P < 0.01$). (**I**) Spine volume versus synaptic surface area (n = 36 spines; r^2 = 0.91). Some small spines lacked synapses, as has been previously reported (*33*). (**J** to **L**) Same as (G) to (I) for a ChR2$^-$ neuron (n = 33 spines; EM versus post, r^2 = 0.88; EM versus pre, r^2 = 0.85; unpaired variance F-test). Spine volume versus synapse area is shown in (L) (n = 39 spines; r^2 = 0.92). Error bars, SEM.

with the hypothesis that synaptic weight is reflected in spine volume (Fig. 2, I and L, and fig. S7).

We investigated the functional signature associated with structural changes to evaluate whether they were consistent with receptive field plasticity measured at the soma. GCaMP6s activity in individual spines was used to measure input-specific receptive fields (Fig. 3, A to C). Spine receptive fields were heterogeneously distributed along dendritic stretches (fig. S8). We hypothesized that sLTP spines should have their receptive field centers overlapping the visual target because of Hebbian plasticity, whereas nearby sLTD spines would have receptive field centers located away from the target because of heterosynaptic, potentially cooperative, plasticity. Spines with receptive fields overlapping the target stimulus indeed increased in volume (Fig. 3, D and E), whereas neighboring spines with receptive fields away from the target were reduced (Fig. 3, D and F). Structural changes were accompanied by consistent changes in GCaMP6s signal amplitude (fig. S9). The average receptive field for sLTP spines was sharp and centered on the target, whereas the average receptive field for sLTD spines was distributed broadly away from and around the target (Fig. 3G). The distribution of sLTP and sLTD spines as a function of their receptive field distance from the target confirmed that as distance increased, the effect on spine size shifted from sLTP to sLTD (Fig. 3H).

We next electroporated SEP-GluA1—an AMPA receptor (AMPAR) subunit 1 tagged with a pH-sensitive form of green fluorescent protein (GFP), Super Ecliptic pHluorin (SEP) (*27*, *28*)—into single neurons to restrict the signal to membrane-inserted receptors, together with ChR2 and a volume-filling marker, DsRed2. Because the GCaMP6s signal would occlude GFP-tagged proteins, we electroporated GCaMP6s alone into neighboring neurons to determine a pairing target location for inducing plasticity in the ChR2$^+$ neuron (Fig. 4A) (neighboring neurons in V1 share a substantial proportion of their subthreshold receptive field; fig. S10). A strong and distinct SEP fluorescence signal was observed at the surface of individual spines (Fig. 4B, left). Comparing changes in SEP-GluA1 enrichment with volume changes in individual spines more than 2 hours after the pairing protocol, we found a significant positive correlation (Fig. 4, C to E). Positive or negative changes in volume thus reflect corresponding modifications of spine synaptic weight through AMPAR expression changes.

Arc, the protein encoded by the immediate gene *Arc*, is involved in AMPAR endocytosis (*29*). Arc preferentially interacts with the inactive β isoform of CaMKII and acts as an inverse tag of plasticity (*30*) that could potentially mediate heterosynaptic depression in dendritic segments (*31*). We used a monomeric enhanced GFP (mEGFP)–tagged Arc (mEGFP-Arc) probe (*30*) to study the molecular dynamics of Arc after the pairing protocol (Fig. 4B, right). Arc enrichment in spines was increased in sLTD spines and decreased in sLTP spines (Fig. 4, C to E). To test whether Arc mediates heterosynaptic depression, we delivered small hairpin RNA (shRNA; figs. S11 and S12) to deplete Arc in single neurons. Neurons in which Arc was knocked down displayed spines filled with SEP-GluA1 (Fig. 4, F and G), which was homogenously distributed along dendrites, compared with control neurons, where SEP-GluA1 was sparsely and focally distributed (Fig. 4H). To relate Arc expression to calcium signaling in spines (*30*) (fig. S13), we additionally knocked down CaMKIIβ (fig. S11). Dendrites with reduced CaMKIIβ displayed reduced spine-specific Arc expression (Fig. 4, I to K). Knockdown of Arc in neurons expressing GCaMP6s and ChR2 prevented displacement of receptive fields toward the target after pairing (Fig. 4L and fig. S12), consistent with impaired functional plasticity (*32*). In contrast to control neurons, the density of sLTP spines was not significantly different

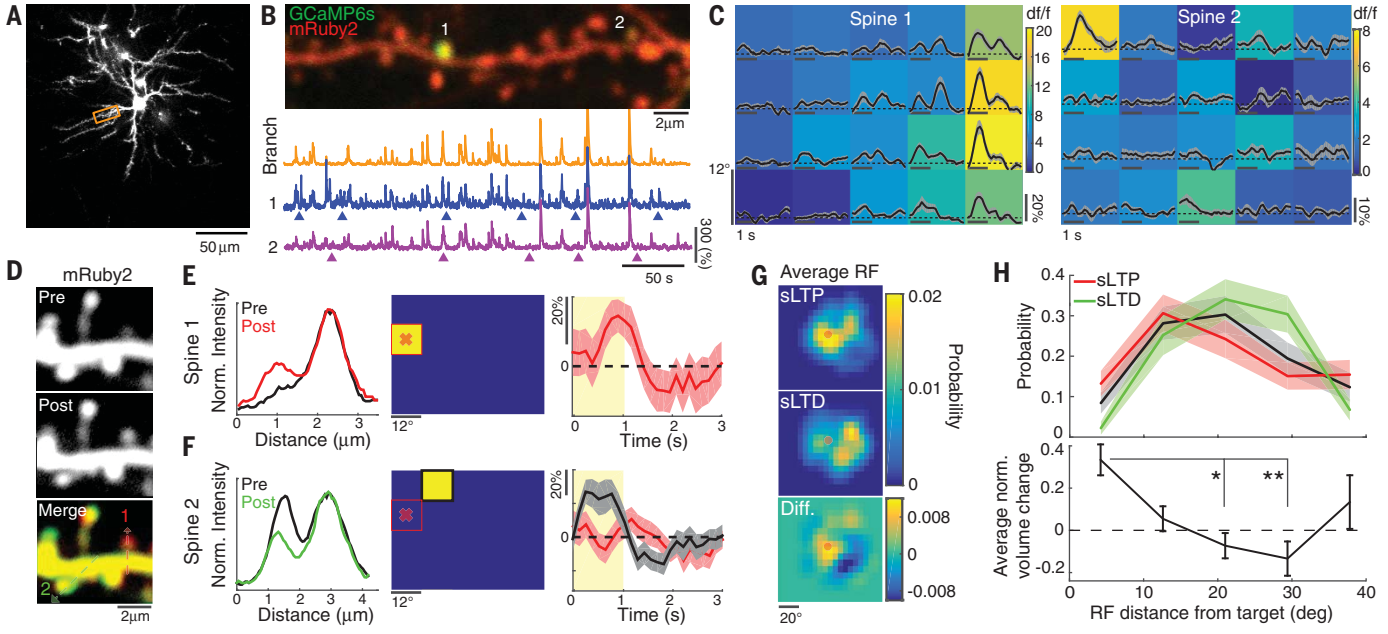

Fig. 3. Functional identification of sLTP and sLTD dendritic spines. (**A**) Neuron expressing mRuby2-P2A-GCaMP6s. (**B**) Top, dendritic stretch from within the rectangle in (A). Bottom, calcium traces for two spines and their corresponding branch. Arrowheads, onset of preferred stimuli. (**C**) Receptive fields for spines in (B). Gray shading, SEM. Color map, time-averaged response. (**D**) Dendritic segment with nearby sLTP ("1") and sLTD ("2") spines. (**E**) Left, profiles from the dashed red line in (D). Middle, receptive field of the spine. Red cross, target position. Right, response time course for the preferred stimulus. Shaded areas, SEM. (**F**) Same as (E) for the sLTD spine in (D). Left, profiles from the dashed green line. Right, response time course for the preferred stimulus (gray) and for the target stimulus location (red). (**G**) Average normalized receptive field centered on the target for sLTP (n = 94) and sLTD (n = 87) spines. Bottom, difference between distributions. (**H**) Top, distribution of receptive field distances from the target. Black distribution, randomized spine identity. Shaded areas, standard deviation. Bottom, average normalized volume change as a function of receptive field distance from the target for all sLTP and sLTD spines (n = 181 spines; one-way ANOVA, $P < 0.01$; *$P < 0.05$ and **$P < 0.01$ with Bonferroni correction). Error bars, SEM.

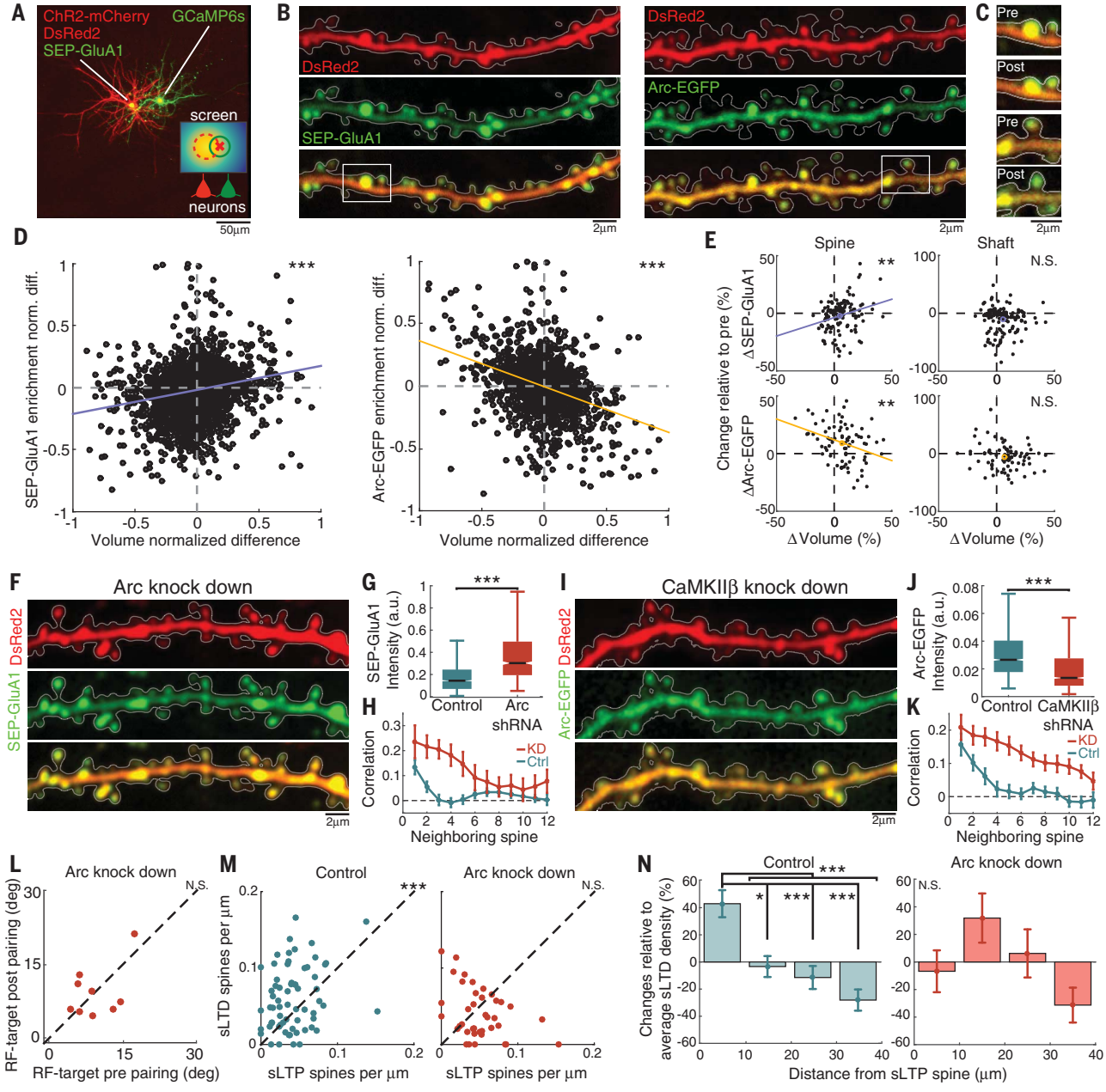

Fig. 4. Role of Arc in regulating plasticity of V1 neurons. (**A**) Neuron expressing ChR2-mCherry, DsRed2, and SEP-GluA1 in close proximity to a neuron expressing GCaMP6s. (**B**) Dendrites expressing SEP-GluA1 (left) or Arc-EGFP (right). (**C**) Spines corresponding to white rectangles in (B). (**D**) Comparison between normalized change in volume and SEP-GluA1 (left) or Arc-EGFP (right) enrichment (SEP-GluA1: n = 4354 spines from 17 neurons, N = 12 mice; Pearson coefficient = 0.22, ***P < 0.001) (Arc-EGFP: n = 1719 spines from 16 neurons, N = 8 mice; Pearson coefficient = −0.37, ***P < 0.001). (**E**) Relative volume changes compared with relative SEP-GluA1 (top; n = 122 dendrites) or Arc-EGFP (bottom; n = 81 dendrites) enrichment changes averaged over all spines or measured in the dendritic shaft (Pearson coefficient = 0.27, **P < 0.01 for SEP-GluA1 and −0.29, **P < 0.01 for Arc-EGFP). Purple and orange lines, best linear fits. Circles, average values. (**F**) Dendrite expressing SEP-GluA1 and Arc shRNA-DsRed2. (**G**) Distributions of spine SEP-GluA1 average intensity when Arc is endogenously expressed or knocked down [n = 960 spines from three neurons for knockdown (KD); n = 2669 spines from 11 neurons for control (Ctrl); Kruskal-Wallis test, ***P < 0.001]. (**H**) SEP-GluA1 intensity correlation with neighboring spines. (**I** to **K**) Same as (F) to (H) in control or CaMKIIβ KD dendrites expressing Arc-EGFP (n = 2053 spines from four neurons for KD; n = 2550 spines from 11 neurons for Ctrl; Kruskal-Wallis test, ***P < 0.001). (**L**) Distance between the target and receptive field pre- and postpairing for the Arc KD condition (n = 9 neurons, N = 7 mice; paired Wilcoxon test). (**M**) sLTP and sLTD spine density per dendrite for control (n = 66 dendrites; Pearson coefficient = 0.31, P < 0.05; paired Wilcoxon test, ***P < 0.001) and Arc KD (n = 39 dendrites; Pearson coefficient = −0.37, P < 0.05; paired Wilcoxon test, not significant) conditions. (**N**) sLTD spine density variation relative to the mean as a function of distance from sLTP spines for the control (average over n = 253 sLTP spines; one-way ANOVA, P < 0.001; unpaired Kruskal-Wallis test, ***P < 0.001 and *P < 0.05 with Bonferroni correction) and Arc KD conditions (average over n = 142 sLTP spines; one-way ANOVA, not significant). Dendrites in the control condition either express a scrambled Arc shRNA plasmid fused with DsRed (n = 46 dendrites) or mRuby2-P2A-GCaMP6s (n = 20 dendrites). Error bars, SEM.

from the density of sLTD spines for neurons with Arc knockdown (Fig. 4M). The spatial organization of sLTD spines around sLTP spines was impaired in Arc knockdown dendrites compared with controls (Fig. 4N), demonstrating that Arc helps organize the distribution of potentiated and depressed spines that underlies plasticity of neuronal responses. Local bidirectional plasticity of functionally identified spines was also observed in experiments where vision from the deprived eye was restored after monocular deprivation (fig. S15). Thus, Arc-mediated heterosynaptic plasticity takes place under physiological conditions and constitutes a mechanism for local coordination of synaptic plasticity that drives functional plasticity of neurons with heterogeneous synaptic inputs (fig. S16).

REFERENCES AND NOTES

1. H. Ko *et al*., *Nature* **496**, 96–100 (2013).
2. J. S. Espinosa, M. P. Stryker, *Neuron* **75**, 230–249 (2012).
3. S. X. Chen, A. N. Kim, A. J. Peters, T. Komiyama, *Nat. Neurosci.* **18**, 1109–1115 (2015).
4. J. Cichon, W.-B. Gan, *Nature* **520**, 180–185 (2015).
5. A. Hayashi-Takagi *et al*., *Nature* **525**, 333–338 (2015).
6. G. G. Turrigiano, S. B. Nelson, *Nat. Rev. Neurosci.* **5**, 97–107 (2004).
7. K. Ibata, Q. Sun, G. G. Turrigiano, *Neuron* **57**, 819–826 (2008).
8. W. Ju *et al*., *Nat. Neurosci.* **7**, 244–253 (2004).
9. W. C. Oh, L. K. Parajuli, K. Zito, *Cell Rep.* **10**, 162–169 (2015).
10. M. A. Sutton *et al*., *Cell* **125**, 785–799 (2006).
11. W.-J. Bian, W.-Y. Miao, S.-J. He, Z. Qiu, X. Yu, *Cell* **162**, 808–822 (2015).
12. J. Winnubst, J. E. Cheyne, D. Niculescu, C. Lohmann, *Neuron* **87**, 399–410 (2015).
13. J. N. Bourne, K. M. Harris, *Hippocampus* **21**, 354–373 (2011).
14. A. Govindarajan, R. J. Kelleher, S. Tonegawa, *Nat. Rev. Neurosci.* **7**, 575–583 (2006).
15. J. C. Béïque, Y. Na, D. Kuhl, P. F. Worley, R. L. Huganir, *Proc. Natl. Acad. Sci. U.S.A.* **108**, 816–821 (2011).
16. Q. Hou, D. Zhang, L. Jarzylo, R. L. Huganir, H.-Y. Man, *Proc. Natl. Acad. Sci. U.S.A.* **105**, 775–780 (2008).
17. M. C. Lee, R. Yasuda, M. D. Ehlers, *Neuron* **66**, 859–870 (2010).
18. I. Rabinowitch, I. Segev,*Trends Neurosci.* **31**, 377–383 (2008).
19. Supplementary materials.
20. C. D. Meliza, Y. Dan, *Neuron* **49**, 183–189 (2006).
21. V. Pawlak, D. S. Greenberg, H. Sprekeler, W. Gerstner, J. N. D. Kerr, *eLife* **2**, e00012 (2013).
22. T. Rose *et al.*, *Science* **352**, 1319–1322 (2016).
23. F. Zhang *et al*., *Nature* **446**, 633–639 (2007).
24. M. Matsuzaki, N. Honkura, G. C. R. Ellis-Davies, H. Kasai, *Nature* **429**, 761–766 (2004).
25. C. D. Harvey, K. Svoboda, *Nature* **450**, 1195–1200 (2007).
26. Y. Zhang, R. H. Cudmore, D.-T. Lin, D. J. Linden, R. L. Huganir, *Nat. Neurosci.* **18**, 402–407 (2015).
27. C. D. Kopec, B. Li, W. Wei, J. Boehm, R. Malinow, *J. Neurosci.* **26**, 2000–2009 (2006).
28. H. Makino, R. Malinow, *Neuron* **72**, 1001–1011 (2011).
29. S. Chowdhury *et al*., *Neuron* **52**, 445–459 (2006).
30. H. Okuno *et al*., *Cell* **149**, 886–898 (2012).
31. C. Mullins, G. Fishell, R. W. Tsien, *Neuron* **89**, 1131–1156 (2016).
32. C. L. McCurry *et al*., *Nat. Neurosci.* **13**, 450–457 (2010).
33. G. W. Knott, A. Holtmaat, L. Wilbrecht, E. Welker, K. Svoboda, *Nat. Neurosci.* **9**, 1117–1124 (2006).

ACKNOWLEDGMENTS

We thank R. Neve, B. Bartelle, and A. Jasanoff for their assistance with plasmid preparation and testing; J. Petravicz for performing the eyelid sutures for monocular deprivation experiments; M. Yildirim for providing two-photon point spread function measurements; K. Li for his assistance with optical intrinsic imaging; O. Marre, J. Mayrhofer, and C. Gasselin for their comments on the manuscript; and V. Jayaraman, R. A. Kerr, D. S. Kim, L. L. Looger, and K. Svoboda from the GENIE Project, Janelia Farm Research Campus, Howard Hughes Medical Institute (HHMI), for the distribution of GCaMP6. **Funding:** This work was supported by Marie Curie postdoctoral fellowship FP7-PEOPLE-2010-IOF (to S.E.-B.), a Human Frontier Science Program Long-Term Fellowship (to J.P.K.I.), AMED-CREST (to H.B.), KAKENHI grants (15H04258 to H.O. and 15H02358 and 17H06312 to H.B.), and NIH grants NS090473 and EY007023, NSF grant EF1451125, the Simons Center for the Social Brain, and the Picower Institute Innovation Fund (to M.S.). **Author contributions:** S.E.-B., J.P.K.I., and M.S. conceived experiments. S.E.-B. performed single-cell electroporation. S.E.-B. and J.P.K.I. performed surgeries and carried out in vivo experiments. S.E.-B. performed data analysis. M.S. and J.P.K.I. contributed to analysis of experiments. V.B.-P. performed intracellular recordings in vivo and eye-tracking controls. G.W.K. performed the EM and analysis. H.O. and H.B. designed and provided the Arc-EGFP plasmid and the CaMKIIβ shRNA and controls. S.E.-B., J.P.K.I., V.B.-P., and M.S. wrote the paper. **Competing interests:** The authors declare no competing interests. **Data and materials availability:** All data needed to evaluate the conclusions of the paper are in the paper or the supplementary materials or are available at www.surlab.org. pGL4.11-Arc7000-mGFP-Arc-UTRs, CaMKIIβ shRNA vector, and control shRNA vector are available from H.B. under a material transfer agreement with the University of Tokyo.

SUPPLEMENTARY MATERIALS

www.sciencemag.org/content/360/6395/1349/suppl/DC1
Materials and Methods
Figs. S1 to S16
References (*34–49*)

13 June 2017; resubmitted 7 March 2018
Accepted 8 May 2018
10.1126/science.aao0862

Locally coordinated synaptic plasticity of visual cortex neurons in vivo

Sami El-Boustani, Jacque P. K. Ip, Vincent Breton-Provencher, Graham W. Knott, Hiroyuki Okuno, Haruhiko Bito and Mriganka Sur

Science **360** (6395), 1349-1354.
DOI: 10.1126/science.aao0862

Rebalancing strength between synapses

Activation of a neuronal pathway is often associated with inhibition of surrounding pathways. How locally coordinated synaptic plasticity occurs in vivo is not known, nor is its role in shaping neuronal responses. El-Boustani *et al.* paired optogenetic stimulation of single neurons with a visual input and were able to shift the neuron's receptive field toward the target location. Spines that expressed structural long-term potentiation had receptive fields overlapping the target stimulus but were surrounded by spines that expressed receptive fields away from the target.

Science, this issue p. 1349